1 # Supporting information:

2 # Physical constraints for respiration in microbial hotspots in soil
3 # and their impact on denitrification

4 Steffen Schlüter[1] , Jan Zawallich[2], Hans-Jörg Vogel[1], Peter Dörsch[3]

5 1. Department Soil System Sciences, Helmholtz-Centre for Environmental Research - UFZ,
6 Halle, Germany

7 2. TU Clausthal, Clausthal-Zellerfeld, Germany

8 3. Norwegian University of Life Sciences, NMBU, As, Norway

1. Supplementary information

1.1.   Methods: Incubation

Figure S1: (a) Half-pint incubation jar (230ml) filled with sand and porous glass beads that serve as microbial hotspots.
(b) Respiration kinetics of different types of hotspots either inoculated with *Agrobacterium tumefaciens* or *Paracoccus*
***denitrificans* are measured with 50 hotspots in an otherwise empty glass jar (120ml). Note that hotspots are packed densely**
with minimal distance, which might have affected aeration.

1.2.   Methods: Product ratios

Ratios of gaseous denitrification products may vary strongly depending on the incubation period
for which they are computed. Moreover, in an experimental setup with a permanently close
headspace, intermediates may temporarily accumulate in the headspace and still be available as
an electron acceptor and diffuse back into the soil at a later incubation stage. This would not be
the case in a continuous flow setup with a carrier gas that lack NO and N_2O and also to a much
lesser extent under natural conditions were the NO and N_2O concentrations are immediately
diluted down to atmospheric concentrations. Still, apparent product ratios can still be computed

24   by adding up the release of intermediates and subtracting this amount from subsequent
25   denitrification product prior to computing ratios. To do so, we define

26    $NO^* := \int_0^T \Theta(no'(t))dt, \ N_2O^* := \int_0^T \Theta(n_2o'(t))dt, \ N_2^* := \int_0^T \Theta(n_2'(t))dt$

27   Where F^* is the cumulative release, T is the end of incubation, f' is the first time derivative of
28   concentration f, and Θ is defined as

$$\Theta := \begin{cases} x & \text{if } x > 0 \\ 0 & \text{else.} \end{cases}$$

29   We then have

30    $NO = NO^*, \ N_2O = N_2O^* - NO^*$ and $N_2 = N_2^* - N_2O^*$.

31   We define the product ratios:

32    $\mathbf{NO} := \frac{NO}{NO+N_2O+N_2}, \ \mathbf{N_2O} := \frac{N_2O}{NO+N_2O+N_2}$ and $\mathbf{N_2} := \frac{N_2}{NO+N_2O+N_2}$.

33   Note that these estimated ratios disregard the actual effects that the presence of NO and N_2O may
34   have on the regulation of enzymes for various denitrification steps. They should therefore only be
35   considered as a rough approximation to product ratios in open systems. One benefit of this
36   approach is that T is identical for all samples and does not have to be adjusted to individual
37   denitrification kinetics.

1.3.   Methods: Image processing and analysis

39   The inner volume of the glass jars filled with quartz sand, water and air constitutes the region of
40   interest (ROI) to be analyzed except for the porous hotspots which are considered as cavities in
41   the ROI. The ROI was determined by semi-automatic region growing in VG StudioMax 2.1
42   (Volume Graphics) based on gradient images, i.e. the first derivative of the original gray scale
43   image. The gradient was approximated by the Variance 3D filter in Fiji/ImageJ. Region growing
44   was initiated on the homogeneous glass wall of the jar and in the homogeneous head space of the
45   jar and stopped directly at the border of the repacked sand. The fully enclosed volume of both
46   region growing processes is considered as ROI. Likewise, region growing in the relatively
47   homogeneous hotspots stopped directly at the border between hotspots and repacked sand. This
48   was used to demarcate the porous glass beads and subtract them from the ROI. The assignment to
49   *At* and *Pd* hotspots was done according to the vertical position in the layered architecture and
50   according to orientation of the flat and rounded end in the random architecture.

51   The raw image were filtered with a non-local means filter (Buades et al., 2005) for noise removal
52   at an estimated noise level of $\sigma = 7$ gray values using the non-local denoising plugin for ImageJ.
53   Edge enhancement was carried out with an unsharp mask filter (Sheppard et al., 2004; Schlüter et
54   al., 2014). A vertical drift in gray values due to uneven illumination was detected and corrected

55 for all voxels by subtracting the difference between the average gray values in sand grain voxels
56 per slice with the average gray value of all sand grain voxels (Iassonov and Tuller, 2010; Schlüter
57 et al., 2016). Thresholds were chosen manually and adjusted to the predefined water saturation
58 within test regions. Simple thresholding was carried out to segment the ROI voxels into air water
59 and solid followed by a majority filter with a cubic 3^3 kernel to remove partial volume effects
60 (Schlüter et al., 2014).

61 These segmented images were analyzed with respect to different morphological properties of the
62 air-filled and water-filled pores space. All properties are reported separately for the complete ROI
63 and the direct neighborhood of the hotspot boundaries to assess the local conditions experienced
64 by the hotspots. The reduced ROI for the hotspot boundaries was created by dilation and
65 subsequent subtraction of the hotspot ROI.

66 Dimensionless air connectivity was determined through the volume fraction of air-filled pores
67 with a continuous path to the headspace. To do so, a connected components labelling was
68 performed with the MorpholibJ plugin in Fiji/ImageJ (Legland et al., 2016) to mask out all air
69 clusters without a connection to the headspace.

70 Air tortuosity was determined in the connected air cluster using the Geodesic Distance map 3D in
71 the MorpholibJ plugin (Legland et al., 2016). This transform writes the shortest path lengths fully
72 within the air cluster from the headspace to any location belong to the air cluster. The
73 dimensionless tortuosity number is then determined for each voxel as the ratio between geodesic
74 distance and depth-dependent, Euclidean distance.

75 Air distance is determined as the shortest, geodesic distance within the water-filled pore space
76 from any water voxel to the closest air voxel belonging to the connected air cluster. This air
77 distance cannot be normalized in a meaningful way and is therefore reported as a length in mm.

78
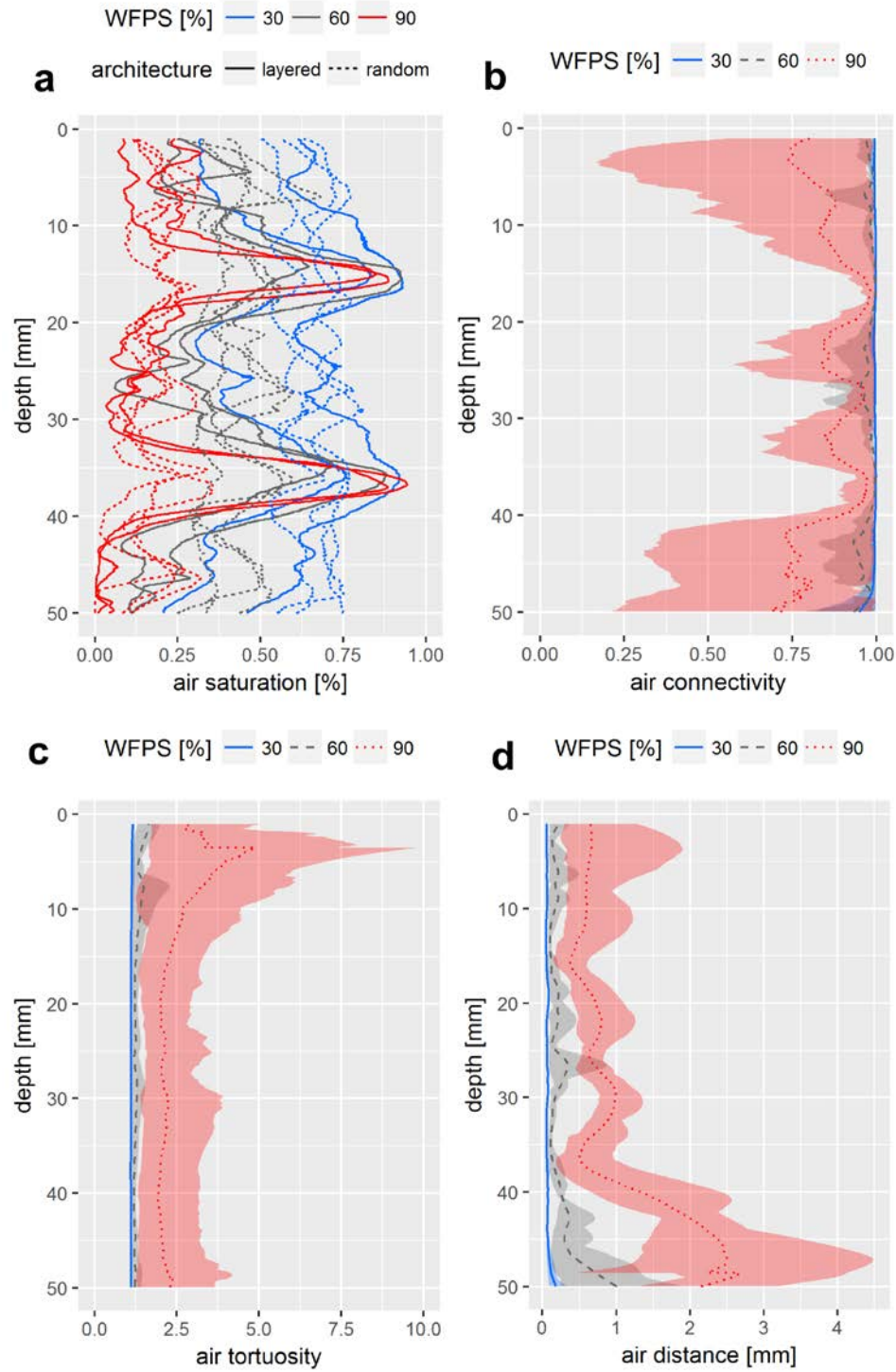
Figure S2: Depth profiles (n=5) of (a) air saturation, (b) air connectivity, (c) air tortuosity and (d) air distance. Individual profiles are shown in (a) two highlight the differences between layered and random architectures that are caused by packing gaps around hotspots. All other profiles (b-d) are shown as averages (lines) with min-max bands (transparent areas).

83
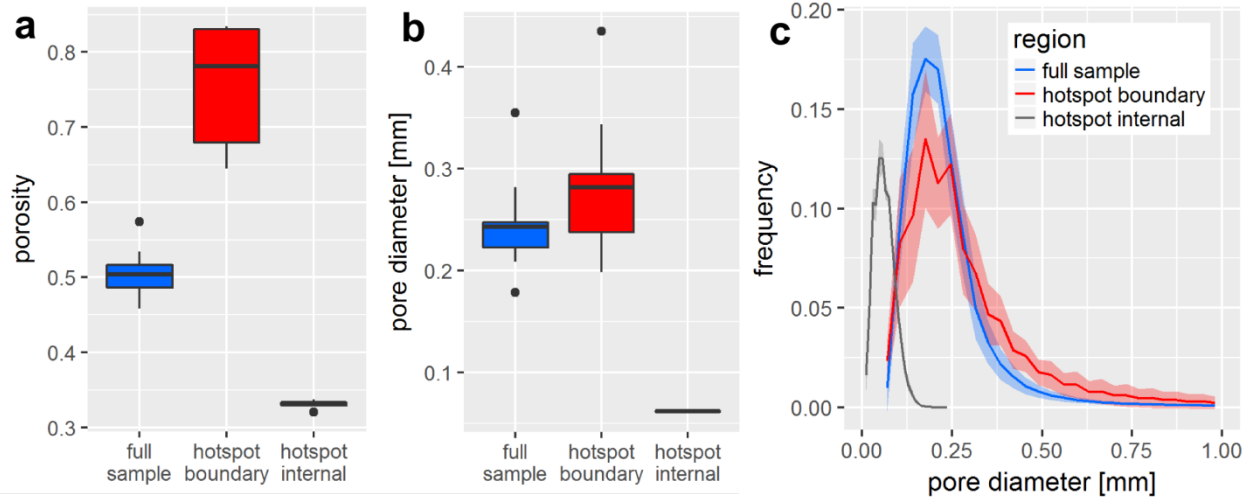
Figure S3: (a) Visible porosity and (b) pore diameter of individual hotspots (n=4) and the incubated sand samples (n=9) reported separately for the full sample or the only the hotspot boundaries affected by packing gaps. (c) The pore size distributions have an overlap at a diameter range of 80-150μm, which explains why liquid is sucked out of the hotspots, when pores <150μm in the sand are air-filled. (a-b): Data shown as box-whisker plots: Whiskers- min-max, middle lines – median, dots: outliers. (c) Lines represent average and transparent bands the min-max range.

90
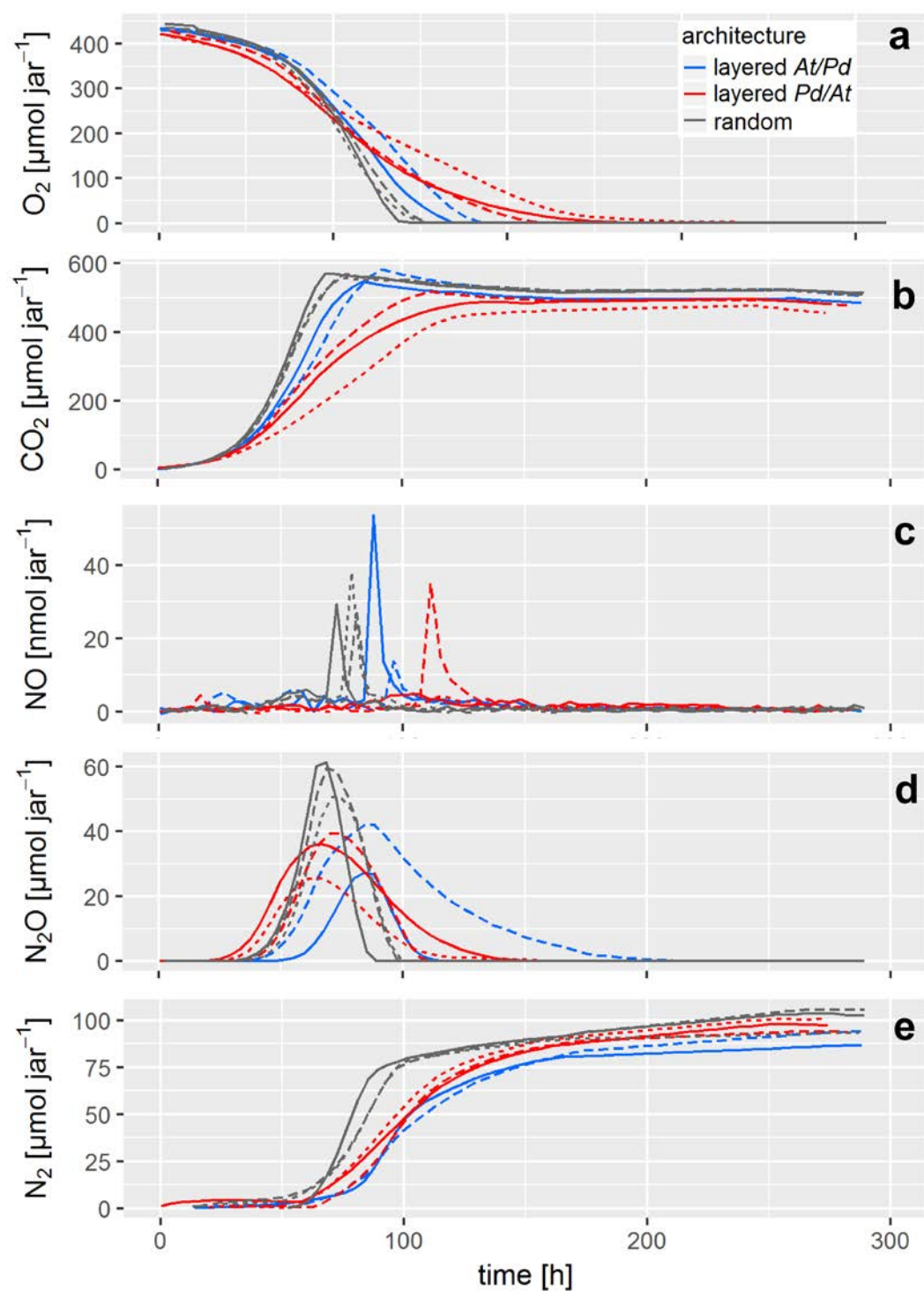
Figure S4: Gas kinetics in all treatments at high saturation (90% WFPS) for three different hotspot architectures: (a) O2, (b) CO2, (c) NO, (d) N2O, (e) N2. Note the logarithmic ordinate in (c) and (d). Different lines styles represent replicates.

1.5. Results: Incubation at 60% saturation
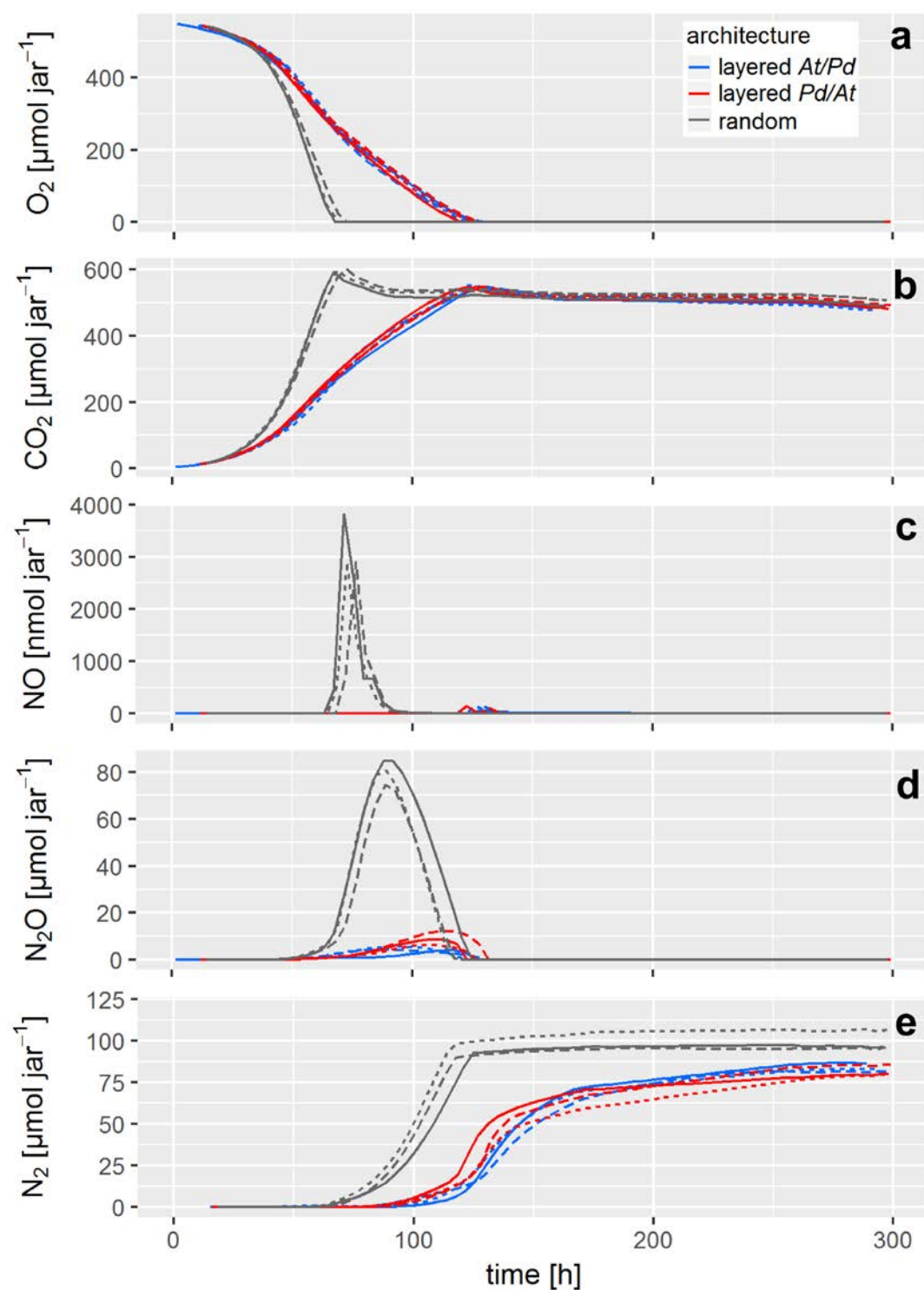
Figure S5: Gas kinetics in all treatments at medium saturation (60% WFPS) for three different hotspot architectures: (a) O2, (b) CO2, (c) NO, (d) N2O, (e) N2. Note the logarithmic ordinate in (c) and (d). Different lines styles represent replicates.

98

100

101   Figure S6: Gas kinetics in all treatments at low saturation (30% WFPS) for three different hotspot architectures: (a) O2,
102   (b) CO2, (c) NO, (d) N2O, (e) N2. Note the logarithmic ordinate in (c) and (d). Different lines styles represent replicates.

103
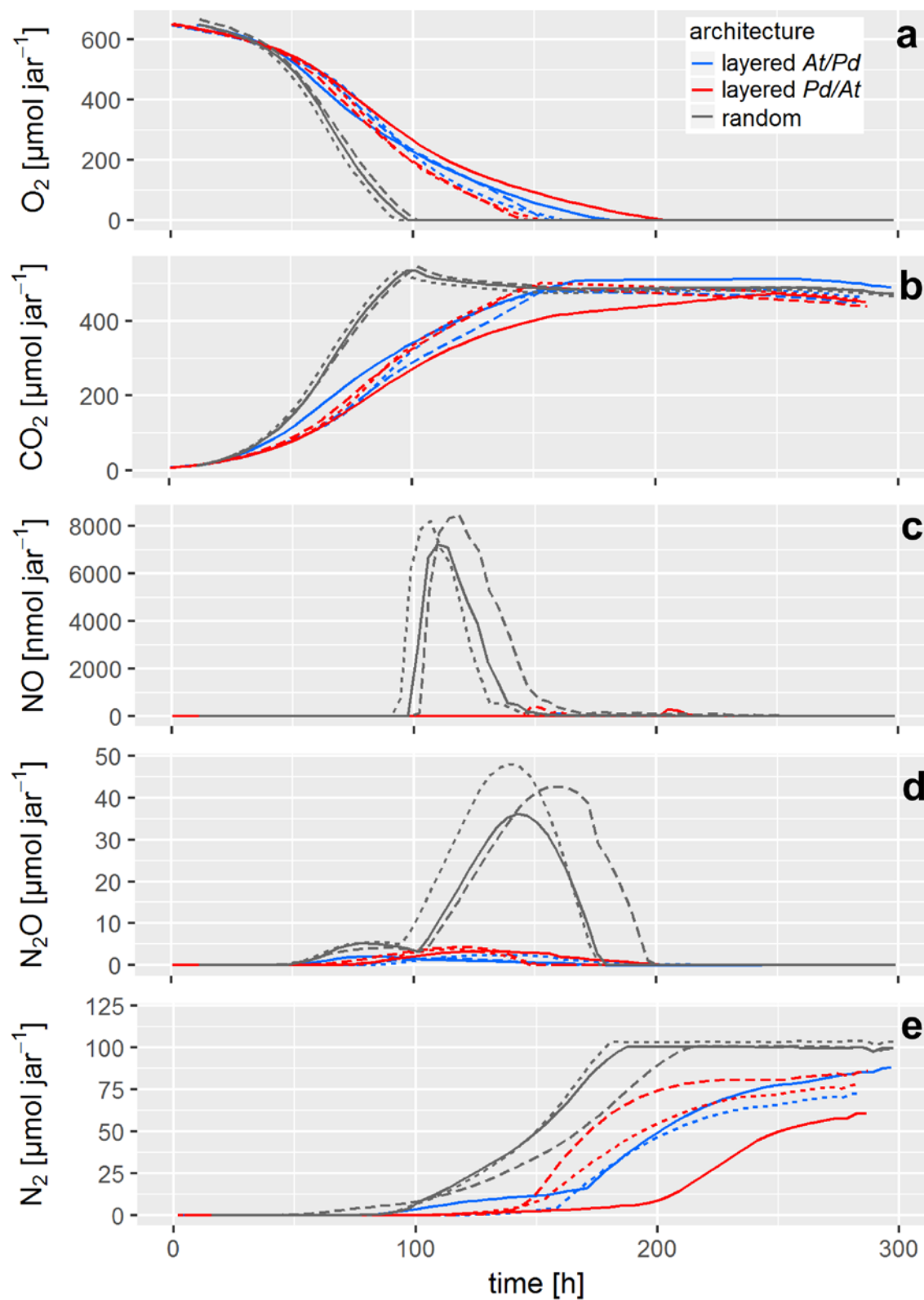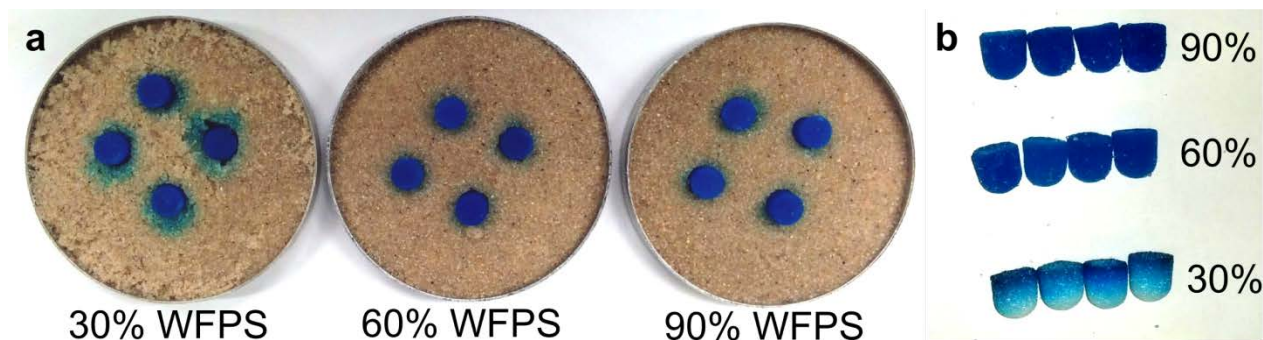
Figure S7: (a) transport of brilliant blue dye from aggregates into sand at different saturations after≈10min. At 30% WFPS transport is dominated by convection, whereas at higher saturation only diffusion remains. (b) dye loss after one day.

1.7.   Results: Nitrogen balance
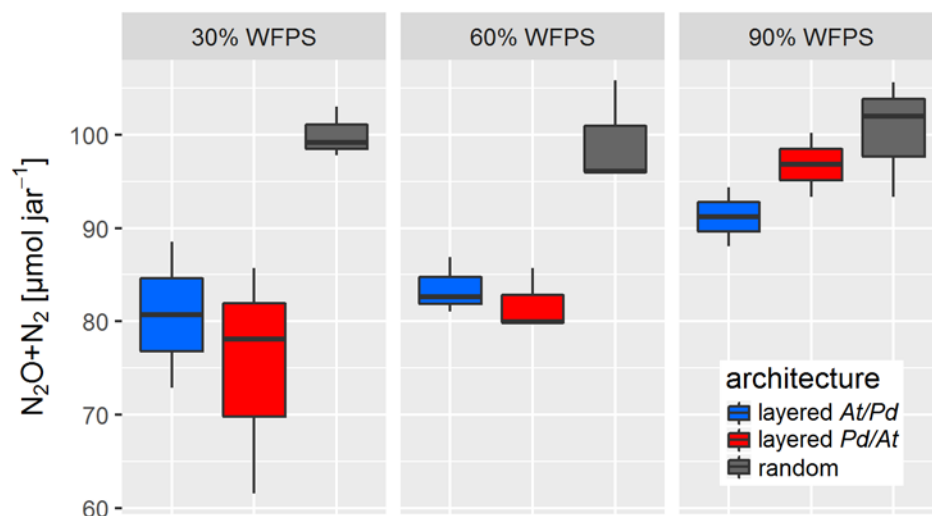
Figure S8: Sum of denitrification products (N_2O, N_2) at the end of incubation (300h) for all architectures and saturations (n=3). The amount of initially present nitrate estimated from the internal porosity of hotspots was 96 µmol NO_3-N per jar, with some additional nitrate in growth medium adhering to the hotspot boundaries by week capillary forces during packing.

1.8.   References

Buades, A., Coll, B., Morel, J.-M., 2005. A non-local algorithm for image denoising, Computer Vision and Pattern Recognition, 2005. CVPR 2005. IEEE Computer Society Conference on, San Diego, California, pp. 60-65 vol. 62.

Iassonov, P., Tuller, M., 2010. Application of segmentation for correction of intensity bias in X-ray computed tomography images. Vadose Zone Journal 9, 187-191.

Legland, D., Arganda-Carreras, I., Andrey, P., 2016. MorphoLibJ: integrated library and plugins for mathematical morphology with ImageJ. Bioinformatics 32, 3532-3534.

Schlüter, S., Leuther, F., Vogler, S., Vogel, H.-J., 2016. X-ray microtomography analysis of soil structure deformation caused by centrifugation. Solid Earth 7, 129-140.

124   Schlüter, S., Sheppard, A., Brown, K., Wildenschild, D., 2014. Image processing of multiphase
125   images obtained via X-ray microtomography: A review. Water Resources Research 50, 3615-
126   3639.
127   Sheppard, A.P., Sok, R.M., Averdunk, H., 2004. Techniques for image enhancement and
128   segmentation of tomographic images of porous materials. Physica A: Statistical Mechanics and
129   its Applications 339, 145-151.

130